Dear Author

Please use this PDF proof to check the layout of your article. If you would like any changes to be made to the layout, you can leave instructions in the online proofing interface. Making your changes directly in the online proofing interface is the quickest, easiest way to correct and submit your proof. Please note that changes made to the article in the online proofing interface will be added to the article before publication, but are not reflected in this PDF proof.

If you would prefer to submit your corrections by annotating the PDF proof, please download and submit an annotatable PDF proof by clicking here and you'll be redirected to our PDF Proofing system.

Nanoscale d0nr04555a

We have presented the graphical abstract image and text for your article below. This briefly summarises your work, and will be presented with your article online.

1

Simultaneous mapping of nanoscale topography and surface potential of charged surfaces by scanning ion conductance microscopy

Feng Chen, Namuna Panday, Xiaoshuang Li, Tao Ma, Jing Guo, Xuewen Wang, Lidia Kos, Ke Hu, Ning Gu* and Jin He*

Simultaneous mapping of nanoscale topography and surface potential of soft, rough and heterogeneously charged surfaces under physiological conditions.

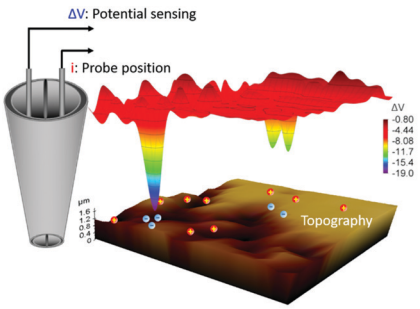

Please check this proof carefully. Our staff will not read it in detail after you have returned it.

Please send your corrections either as a copy of the proof PDF with electronic notes attached or as a list of corrections. **Do not edit the text within the PDF or send a revised manuscript** as we will not be able to apply your corrections. Corrections at this stage should be minor and not involve extensive changes.

Proof corrections must be returned as a single set of corrections, approved by all co-authors. No further corrections can be made after you have submitted your proof corrections as we will publish your article online as soon as possible after they are received.

Please ensure that:

- The spelling and format of all author names and affiliations are checked carefully. You can check how we have identified the authors' first and last names in the researcher information table on the next page. **Names will be indexed and cited as shown on the proof, so these must be correct.**
- Any funding bodies have been acknowledged appropriately and included both in the paper and in the funder information table on the next page.
- All of the editor's queries are answered.
- Any necessary attachments, such as updated images or ESI files, are provided.

Translation errors can occur during conversion to typesetting systems so you need to read the whole proof. In particular please check tables, equations, numerical data, figures and graphics, and references carefully.

Please return your **final** corrections, where possible within **48 hours** of receipt following the instructions in the proof notification email. If you require more time, please notify us by email to nanoscale@rsc.org.

Funding information

Providing accurate funding information will enable us to help you comply with your funders' reporting mandates. Clear acknowledgement of funder support is an important consideration in funding evaluation and can increase your chances of securing funding in the future.

We work closely with Crossref to make your research discoverable through the Funding Data search tool (http://search.crossref.org/funding). Funding Data provides a reliable way to track the impact of the work that funders support. Accurate funder information will also help us (i) identify articles that are mandated to be deposited in **PubMed Central (PMC)** and deposit these on your behalf, and (ii) identify articles funded as part of the **CHORUS** initiative and display the Accepted Manuscript on our web site after an embargo period of 12 months.

Further information can be found on our webpage (http://rsc.li/funding-info).

What we do with funding information

We have combined the information you gave us on submission with the information in your acknowledgements. This will help ensure the funding information is as complete as possible and matches funders listed in the Crossref Funder Registry.

If a funding organisation you included in your acknowledgements or on submission of your article is not currently listed in the registry it will not appear in the table on this page. We can only deposit data if funders are already listed in the Crossref Funder Registry, but we will pass all funding information on to Crossref so that additional funders can be included in future.

Please check your funding information

The table below contains the information we will share with Crossref so that your article can be found *via* the Funding Data search tool. **Please check that the funder names and grant numbers in the table are correct and indicate if any changes are necessary to the Acknowledgements text.**

Funder name	Funder's main country of origin	Funder ID (for RSC use only)	Award/grant number
Q1 National Science Foundation	United States	100000001	CBET1454544 EEC-1647837
China Sponsorship Council	China	501100004543	Unassigned
Florida International University	United States	100007681	Unassigned

Researcher information

Please check that the researcher information in the table below is correct, including the spelling and formatting of all author names, and that the authors' first, middle and last names have been correctly identified. **Names will be indexed and cited as shown on the proof, so these must be correct.**

If any authors have ORCID or ResearcherID details that are not listed below, please provide these with your proof corrections. Please ensure that the ORCID and ResearcherID details listed below have been assigned to the correct author. Authors should have their own unique ORCID iD and should not use another researcher's, as errors will delay publication.

Please also update your account on our online manuscript submission system to add your ORCID details, which will then be automatically included in all future submissions. See here for step-by-step instructions and more information on author identifiers.

First (given) and middle name(s)	Last (family) name(s)	ResearcherID	ORCID iD
Feng	Chen		
Namuna	Panday		
Xiaoshuang	Li		
Tao	Ma		
Jing	Guo		
Xuewen	Wang		

Lidia	Kos		
Ke	Hu		
Ning	Gu		0000-0002-2633-9809
Jin	He		0000-0002-2633-9809

Queries for the attention of the authors

Journal: **Nanoscale** Paper: **d0nr04555a**

Title: **Simultaneous mapping of nanoscale topography and surface potential of charged surfaces by scanning ion conductance microscopy**

For your information: You can cite this article before you receive notification of the page numbers by using the following format: (authors), Nanoscale, (year), DOI: 10.1039/d0nr04555a.

Editor's queries are marked like this Q1, Q2, and for your convenience line numbers are indicated like this 5, 10, 15, ...

Please ensure that all queries are answered when returning your proof corrections so that publication of your article is not delayed.

Query Reference	Query	Remarks
Q1	Funder details have been incorporated in the funder table using information provided in the article text. Please check that the funder information in the table is correct.	
Q2	ORCID iD 0000-0002-2633-9809 has been provided for more than one author of this paper. Please check and confirm which author this ORCID iD should be associated with. Please note that each ORCID iD is a unique researcher identifier that allows you to link your research output and other professional activities in a single record.	
Q3	Please confirm that the spelling and format of all author names is correct. Names will be indexed and cited as shown on the proof, so these must be correct. No late corrections can be made.	
Q4	The meaning of the phrase "nanoscale cell membrane and bioelectricity" in the sentence beginning "This P-SICM method..." is not clear. Please provide alternative text.	
Q5	The sentence beginning "To change the surface..." has been altered for clarity. Please check that the meaning is correct.	
Q6	The sentence beginning "To increase the..." has been altered for clarity. Please check that the meaning is correct.	
Q7	The sentence beginning "In the $I-t$ traces..." has been altered for clarity. Please check that the meaning is correct.	
Q8	In the sentence beginning "Because of the..." a word or phrase appears to be missing after "image". Please check this carefully and indicate any changes required here.	
Q9	The sentence beginning ". Statistically, the ΔV histogram..." has been altered for clarity. Please check that the meaning is correct.	
Q10	The sentence beginning "In the next step..." has been altered for clarity. Please check that the meaning is correct.	
Q11	Ref. 18: Please provide the page (or article) number(s).	

Nanoscale

PAPER

Simultaneous mapping of nanoscale topography and surface potential of charged surfaces by scanning ion conductance microscopy†

Cite this: DOI: 10.1039/d0nr04555a

Feng Chen,[a,b] Namuna Panday,[b] Xiaoshuang Li,[c] Tao Ma,[b,d] Jing Guo,[b] Xuewen Wang,[b] Lidia Kos,[c,e] Ke Hu,[a] Ning Gu *[a,f] and Jin He *[b,e]

Scanning ion conductance microscopy (SICM) offers the ability to obtain nanoscale resolution images of the membranes of living cells. Here, we show that a dual-barrel nanopipette probe based potentiometric SICM (P-SICM) can simultaneously map the topography and surface potential of soft, rough and heterogeneously charged surfaces under physiological conditions. This technique was validated and tested by systematic studies on model samples, and the finite element method (FEM) based simulations confirmed its surface potential sensing capability. Using the P-SICM method, we compared both the topography and extracellular potential distributions of the membranes of normal (Mela-A) and cancerous (B16) skin cells. We further monitored the structural and electrical changes of the membranes of both types of cells after exposing them to the elevated potassium ion concentration in extracellular solution, known to depolarize and damage the cell. From surface potential imaging, we revealed the dynamic appearance of heterogeneity of the surface potential of the individual cell membrane. This P-SICM method provides new opportunities to study nanoscale cell membrane and bioelectricity.

Received 16th June 2020,
Accepted 7th September 2020
DOI: 10.1039/d0nr04555a
rsc.li/nanoscale

1. Introduction

Imaging the fine structures of living cell membranes is a challenging task. The ultrathin cell membrane is transparent for optical microscopy. Atomic force microscopy (AFM) is a better surface imaging technique to reveal the nanoscale cell membrane structures. However, the physical contact between the AFM probe and cell inevitably impairs its delicate membrane and makes passive observations of the cell surface dynamics difficult.[1,2] Scanning ion conductance microscopy (SICM) is an emerging scanning probe microscopy technique, using a glass nanopipette to scan the surface of samples submerged in an electrolyte solution.[3–5] A constant electric bias is applied across the orifice of the nanopipette, resulting in a probe–sample distance sensitive ionic current, which is used as the feedback signal for surface imaging. The working distance is typically in the range of tens of a nanometer, allowing the acquisition of a topography image without physically touching the surface.[6] Because of its robust ionic current based feedback mechanism, SICM is suitable for biological applications under physiological conditions.[7–13] Under these conditions, the ionic current is relatively insensitive to the surface charge and the substrate topography can be acquired.[14] Recently, important progress has been made to enlarge the imaging scale[15] and improve the imaging speed[16,17] of SICM, enabling better imaging of the dynamics of the cell, multicellular structures and tissue.

In addition to topography imaging, SICM is uniquely multifunctional[18] and can also provide other useful information, such as electrochemical activities,[19,20] ion channel distributions,[13,21] mechanical properties[6] and surface charge mapping.[14,22,23] It is a huge challenge to map the nanoscale surface charge distribution of a delicate interface in an electrolyte with high ionic strength. Recent works suggest that SICM is a promising imaging tool for surface charge imaging of complicated biological samples, including cell membranes and tissue surfaces. For example, Perry *et al.* reported simultaneous

[a]School of Biomedical Engineering and Informatics, Nanjing Medical University, Nanjing 211166, People's Republic of China
[b]Physics Department, Florida International University, Miami, FL 33199, USA. E-mail: jinhe@fiu.edu
[c]Department of Biological Science, Florida International University, Miami, FL 33199, USA
[d]School of Chemistry and Chemical Engineering, Wuhan University of Science and Technology, Wuhan, Hubei, 430081, China
[e]Biomolecular Science Institute, Florida International University, Miami, FL 33199, USA
[f]Jiangsu Key Laboratory for Biomaterials and Devices, School of Biological Sciences and Medical Engineering, Southeast University, Nanjing 210009, People's Republic of China. E-mail: guning@esu.edu.cn

†Electronic supplementary information (ESI) available. See DOI: 10.1039/d0nr04555a

mapping of both the topography and surface charge of living Zea root hair cells with a bias modulated SICM.[24] They recorded the current images of the root hair cell and converted them to a surface charge map with the help of simulations. The same group further developed a simplified method, pulse-potential SICM, to map the surface charge of live P12 cells.[25] Klausen *et al.* revealed the capability of SICM for mapping the surface charge density of lipid bilayers from a height difference by subtracting two sequentially acquired topography images at the positive bias and negative bias, respectively. However, it is difficult to monitor dynamic changes of a charged surface by this method.[23] Zhou *et al.* reported a potentiometric SICM (P-SICM) technique for direct potential imaging of a synthetic nanopore, but simultaneous mapping of topography and potential image of a live cell has not been reported yet.[26] The setup also used an electrochemical potentiostat with five electrodes, which is difficult to implement. Although promising, the development of SICM for surface charge/potential distribution mapping of the living cell is still in the primitive phase.

We have simplified the P-SICM setup by just using a dual-barrel nanopipette as the potential probe to detect the open-circuit potential (OCP) near the apex of the nanopipette tip[27] when the tip is scanned in the approach–retract scan (ARS) mode (similar to the hopping mode).[28,29] In this report, we conducted systematic evaluation of this method by varying the imaging parameters on a soft polydimethylsiloxane (PDMS) based model substrate with heterogeneous charge distribution. It is obvious that the surface charge/potential detection using the OCP signal is more sensitive than using current signal. The experimental results were examined by Finite Element Method (FEM) based numerical simulations. We then utilized the P-SICM technique to simultaneously map the topography and surface potential distributions of a living cell membrane. We acquired the extracellular membrane potential distribution of living melanocyte and melanoma cells, and further monitored the membrane topography and extracellular potential changes of both cells after exposing them to high extracellular potassium concentrations. These results highlight the future application of P-SICM for live cell imaging.

2. Experimental

2.1 Materials

All chemicals were purchased from Sigma Aldrich, unless mentioned otherwise. All aqueous solutions were prepared using deionized water (~18 MΩ) from a water purification system (Ultra Purelab System, ELGA/Siemens). Phosphate buffered saline (PBS) at pH 7.2 was prepared with the following composition (in mM): NaCl 137, KCl 2.7, KH_2PO_4 1.5, and Na_2HPO_4 4.3. The 4-(2-hydroxyethyl)-1-piperazineethanesulfonic acid (HEPES) buffer solution contained (in mM): NaCl 143; KCl 5; $CaCl_2$ 2.5; $MgCl_2$ 1.2; HEPES 10; glucose 10. All purchased chemicals and solvents were used without further purification.

2.2 Nanopipette fabrication

Quartz theta capillaries (FG-G QT120-90-7.5, Sutter Instrument) were first cleaned with piranha solution (3 : 1 mixture of sulfuric acid and 30% hydrogen peroxide) for 30 minutes, rinsed repeatedly with deionized water, and dried in an oven at 120 °C overnight. Large and small diameter dual-barrel nanopipettes with pore diameters close to 160 nm and 60 nm, respectively, were prepared from the quartz theta capillaries using a laser pipette puller (P-2000, Sutter Instrument). The pore size at the apex was determined by the ionic current measurement and confirmed by scanning electron microscopy (SEM) images (see Fig. 1(b) and S1†).

2.3 Instrumentation of P-SICM

A commercial SICM (XE-Bio, Park Systems) was modified for the P-SICM setup as shown in Fig. 1(a). A dual-barrel quartz nanopipette was used as the probe. The electrolyte solution filled in both barrels of the nanopipette was the same as the bath solution. Two Ag/AgCl wire electrodes were inserted into both electrolyte-filled barrels and one Ag/AgCl pellet electrode was immersed in the bath solution. One barrel was used for the ionic current measurement and was wired to a current amplifier (Femto DLPCA-200) with a 10^9 × gain, and the other barrel was used for the potential measurement and was wired to a battery powered high input impedance differential amplifier with a 10 × gain. In the typical setup, a constant sample bias V_s was applied to the Ag/AgCl pellet electrode in the bath solution while the Ag/AgCl wire electrode inside the current sensing barrel was grounded. For comparison, a constant tip bias V_t was also applied to the Ag/AgCl wire electrode inside the current sensing barrel while the bath solution was grounded.

We acquired the potential images based on the ARS mode. In the coarse approach step, the probe first approaches vertically from about 6 μm height from the surface to a position with 1% current decrease, corresponding to a probe-to-substrate distance (D_{ps}) slightly over a micron. The SICM images were then constructed based on the repeated fine approach of the probe by controlling the current drop. For each pixel, the probe approaches with a speed about 65 μm s^{-1} from the initial position (the maximum D_{ps}, $D_{ps\text{-}max}$) and stops at the minimum D_{ps} ($D_{ps\text{-}min}$) when the current reduction exceeds the 2% set-point. The $D_{ps\text{-}min}$ is about several tens of a nm. Then, the tip is withdrawn back to the initial position $D_{ps\text{-}max}$ and horizontally moved about 156 nm to the next pixel. It typically takes about 20 minutes to finish one 20 × 20 μm image (with 128 × 128 pixels, unless specified otherwise).

A digital oscilloscope (Yokogawa DL850 scope reader) was used to record the Z position (from the Z piezo strain gauge sensor), current, and potential signals at a sampling rate of 5 kHz. The bandwidth setting in the oscilloscope is 500 Hz for the Z position and 400 Hz for the potential. In the recorded signals, we can observe a small-time delay (<2 ms) between Z and I or V, which is typical for the ARS mode SICM.[30,31] The delay is induced by the processing time of the feedback system, such as current denoise and Z piezo response time, and is longer on the rougher surface.

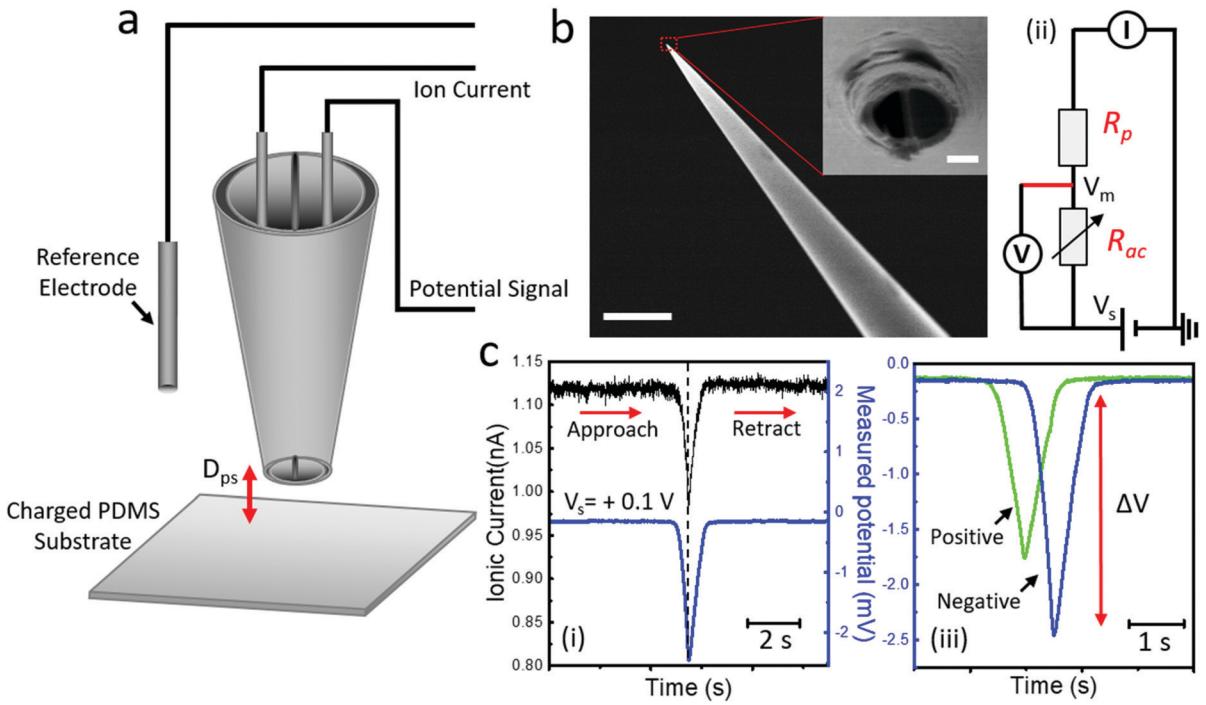

Fig. 1 Simultaneous topographical and potential imaging by the P-SICM method. (a) Schematic of the P-SICM configuration with a dual barrel theta nanopipette as the probe. (b) SEM image of the side-view of a typical large size nanopipette tip (scale bar: 5 μm). The inset shows the apex of the nanopipette, showing two pores with a diameter of about 160 nm each (scale bar: 100 nm). (c) Simultaneously acquired approach-withdraw curves for ionic current (black) and potential (blue) on a negatively charged PDMS substrate in 1× PBS (i). The equivalent circuit for the potential measurement with sample bias (ii). The acquired curves of surface potential on positively (green) and negatively charged (blue) PDMS substrates (iii). Large size nanopipette similar to (b) was used with V_s = +0.1 V.

2.4 Surface modification of PDMS substrates

The PDMS substrate was prepared by mixing 10 parts of the silicone elastomer base and 1 part of the curing agent (SYLGARD, Dow Corning, USA) in a plastic Petri dish, which was partially cured at room temperature after two days. The steps of PDMS surface modification are illustrated in Fig. S2.† To modify bovine serum albumin (BSA), the PDMS substrates were first treated with oxygen plasma for 5 min (Harrick Plasma-PDC 001) and then immersed in 5% 3-aminopropyltriethoxysilane (APTES) solution at room temperature for 1 h. After rinsing with DI water, the substrates were sequentially immersed in 0.5% glutaraldehyde (Glu) solution for 1 h and 5% BSA solution for 3 h. The BSA modified substrates were then rinsed with DI water and dried in a gentle Ar flow. To prepare Au/PDMS substrates, a gold layer was deposited onto the PDMS surface by a reported method.[32] Briefly, the PDMS substrates were immersed in a solution containing 20 mM $HAuCl_4$, 0.5 M $KHCO_3$, and 25 mM glucose at 45 °C until a visible golden layer was formed on the surface. To modify gold with 4-mercaptobenzoic acid (4-MBA) or 4-aminothiophenol (4-ATP), the Au/PDMS substrates were immersed in 1 mM 4-MBA or 4-ATP ethanol solution overnight.

2.5 Cells culture

Mela-A, an immortalized mouse melanocyte cell line (a kind gift from Dr William J. Pavan, NIH),[33] was cultured in RPMI 1640 supplemented with 10% fetal bovine serum, 100 U ml^{-1} penicillin, 100 U ml^{-1} streptomycin, 200 nM TPA and 200 pM cholera toxin at 37 °C in 10% CO_2. The B16-F10, a mouse melanoma cell line (ATCC, CRL-6322), was cultured in Dubelcco's Modified Eagle's Medium (DMEM) supplemented with 10% fetal bovine serum, 100 U ml^{-1} penicillin, and 100 U ml^{-1} streptomycin at 37 °C in 5% CO_2.

2.6 Cell imaging substrates

A PDMS substrate was sterilized in an autoclave and incubated with 50 μg ml^{-1} fibronectin (Gibco) in PBS. The fibronectin solution was dried on the PDMS surface for around 45 min at room temperature. Then the fibronectin modified PDMS was rinsed with PBS before seeding the cells. The cells adhered to the fibronectin-coated-PDMS substrates. Both cells were seeded at low confluency to allow single-cell measurements, and dead cells were removed the next day after cell seeding by changing the medium. The cells were cultured for at least 36 h before experiments. P-SICM experiments of the living cell were performed in HEPES buffer at 37 °C.

2.7 Data analysis

Data analysis was carried out using XEI (Park Systems), Gwyddion, LabVIEW, and Origin Pro (OriginLab Corp.). The potential difference images were constructed using LabVIEW programs; the 3D topography and enhanced color images were

analyzed by XEI; and the surface roughness was analyzed using Gwyddion. To include cell to cell and batch to batch variations, we collected data from at least two cells of each batch and repeated this for at least three batches.

2.8 Finite element method (FEM) simulations

We used FEM simulation to solve coupled Poisson–Nernst–Planck (PNP) partial differential equation. To simplify the simulation, fluidic flow term was not included, and the system was assumed to be in a steady state. COMSOL Multiphysics 5.2 with AD/DC and Chemical Reaction Engineering modules were used for FEM simulation. Details of the simulation are given in the ESI.†

3. Results and discussion

3.1 Validation of surface potential measurement by P-SICM

An illustration of the P-SICM setup for topography and surface potential imaging is shown in Fig. 1(a) and explained in the Experimental section. We used nanopipettes with two different sizes. Fig. 1(b) shows the side view and the top view (right inside) SEM images of a dual-nanopore nanopipette tip with a large pore diameter of about 160 nm. In the top view image, a separation between two similar sized pores can be barely resolved. The SEM images of a nanopipette tip with a small diameter of about 60 nm are shown in Fig. S1.† For experiments, soft deformable PDMS substrates were prepared. To change the surface charge, APTES and BSA have been used to modify the PDMS substrates (see the Experimental methods and section ESI-2†). In 1× PBS solution, the APTES-PDMS substrate provides a positively charged surface, whereas the BSA-PDMS provides a negatively charged surface.[34]

To understand the potential detection mechanism, we first collected both current and potential signals during the approach-withdraw motion of the nanopipette tip at different locations of the PDMS substrates. Fig. 1(c) shows the typical results by a large size nanopipette with V_s = +0.1 V. As shown in Fig. 1(c(i)), both current (black) and potential (blue) time traces are recorded during the experiment. The potential time trace shows the changes in the potential detected using a potential sensing barrel. When the nanopipette tip is far from the substrate (*i.e.*, 0.5 μm), the local potential at the apex is almost the same as the potential of the bath solution. As the probe apex approaches close to the substrates, the ionic current decreases and the potential quickly drops, owing to the increased access resistance R_{ac} induced by the hindered ion flow at a smaller D_{ps}. The overall D_{ps}-dependent changes of both the ionic current and potential can be understood based on the voltage divider model using a simplified equivalent circuit diagram shown in Fig. 1(c(ii)). In the circuit, the potential sensing probe detects the potential at the point between R_{ac} and R_{pore}. The R_{ac}, which is inversely proportional to D_{ps}, is connected in series with R_{pore}, which is determined by the nanopore geometry and can be treated as a constant. During the approach, the decrease of D_{ps} leads to the increase of R_{ac}, and thus the decrease of the current and the potential magnitudes measured by the probe apex. The D_{ps}-dependent changes are shown as the current and potential dips in the approach/withdraw curves in Fig. 1(c(i)). It is apparent that the noise in the potential curve is much smaller than that in the current curve. It should be noted that the $D_{ps\text{-}min}$ is slightly changed because the current at the $D_{ps\text{-}min}$ is affected by the surface charge of the substrate.[14,23] For example, at the positive V_s, the $D_{ps\text{-}min}$ may be bigger on a positively charged surface than on a negatively charged surface. We found that the potential probe could directly sense the change of local potential near the apex, which was affected by the substrate surface charge (see FEM simulation in the next section). One typical result is shown in Fig. 1(c(iii)). We defined ΔV, which is the difference in the potentials at the $D_{ps\text{-}min}$ and $D_{ps\text{-}max}$ in an approach/withdraw cycle. On a negatively charged PDMS substrate, the ΔV is about −2.3 mV. On a positively charged substrate, the shape of the potential dip is the same but the magnitude of ΔV is reduced to about −1.6 mV. This surface charge dependent ΔV changes can be utilized for surface charge mapping.

We carried out systematic studies to test both positive/negative V_s and V_t by collecting current/potential approach/withdraw curves over different charged substrates. The results are shown in Fig. S5.† In summary, the D_{ps}-dependent ionic current and potential changes are affected by the polarity and mode of the applied bias as well as the charge on the substrates. The applied positive V_s produced bigger ΔV values than the negative V_s. In addition, the positive (negative) V_s typically induce similar ΔV as the negative (positive) V_t. Compared with the large size nanopipette, the small size nanopipette shows a much higher sensitivity to the surface charge and bigger ΔV changes are observed. This is attributed to the smaller $D_{ps\text{-}min}$ of the small size nanopipette during imaging. Importantly, the same surface charge difference always resulted in a better signal-to-noise ratio in ΔV signals than the current. Therefore, ΔV can be used to generate surface charge images with higher sensitivity.

The topography and ΔV images of APTES and BSA modified flat PDMS substrates, respectively, were also acquired by P-SICM, as shown in Fig. S6.† The ΔV images will be further discussed in section 3.3. The ΔV histograms built from the ΔV images are shown in Fig. S6(c).† The negative shift of the ΔV histogram of the more negative BSA-modified substrate is evident while the topography of both surfaces are similar. Therefore, P-SICM is sensitive to the surface charge of the flat substrates.

3.2 FEM simulations

To better understand the experimental results of ΔV changes over charged surfaces, we performed numerical simulations by FEM to solve Poisson–Nernst–Planck (PNP) equations. The details of FEM simulation and extra simulation results can be found in ESI section-7.† A nanopore–nanoelectrode was placed at different distances (D_{ps}) from a charged surface and both the ionic current through the nanopore and the potential

changes on the floating nanoelectrode surface were calculated. The ionic current through the nanopore has been well-studied.[21] Here, we focus on the potential changes. As shown in Fig. S7(d),† we simulated the potential approach curves by changing the D_{ps} from 900 nm to 30 nm. The potential approach curves were simulated on substrates with different surface charge densities. The shape of these potential approach curves is similar to the experimental results shown in Fig. 1(c) at the tip approach region. The V becomes more negative with the decrease of D_{ps}, and can be affected by the substrate surface charge up to about 200 nm. Because of the strong screening effect under physiological conditions, the surface charge cannot directly affect the potential probe. However, the sample surface potential can affect R_{pore}, R_{ac} and the local potential distribution near the floating potential probe, especially when V_s is applied.

ΔV is calculated as the difference between two potential values at $D_{ps\text{-}min}$ (30 nm for a small size nanopipette and 80 nm for a large size nanopipette) and $D_{ps\text{-}max}$ (900 nm for both size nanopipettes), respectively. ΔV_s as a function of the surface charge density is plotted for both the large size nanopipette (Fig. 2(a)) and small size nanopipette (Fig. 2(b)). The ΔV is always more negative at the negatively charged surface and more positive at the positively charged surface, confirming that ΔV is sensitive to the surface charge. The changes of ΔV under different bias conditions were also investigated. The plot with +0.1 V_s is the same as the plot with −0.1 V_t, with all negative ΔV values of the surface charge density ranging from −0.1 to 0.1 C m^{-2}. Likewise, the plot with −0.1 V_s is the same as the plot with +0.1 V_t, with all positive ΔV values in the same surface charge density range. These results corroborate the experimental observations we discussed earlier (see Fig. S5†). Regarding the effect of nanopore sizes of the nanopipette, compared with the big size nanopipette (160 nm diameter), the small size nanopipette (60 nm diameter) shows a slightly increased ΔV response to the surface charge. However, in the experiment, the small size nanopipette can produce a much bigger change in ΔV. The $D_{ps\text{-}min}$ for the small size nanopipette is likely smaller in the experiment than in simulation, thus improving the experimental sensitivity. The fluidic movement induced by the movement of the nanopipette tip may also reduce the screening effect of the double layer and this effect may be more obvious at a smaller $D_{ps\text{-}min}$.

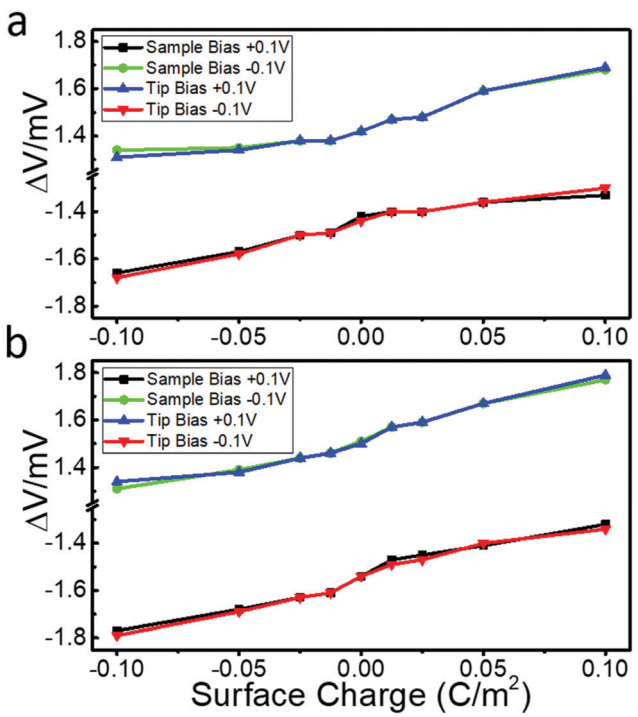

Fig. 2 The simulated ΔV with different bias modulations as a function of the substrate surface charge density under different bias application modes. The results from the large size nanopipette (a, 160 nm diameter) and small size nanopipette (b, 60 nm diameter) models.

3.3 Performance of P-SICM on complicated surfaces

To further examine the capability of P-SICM for imaging complex and soft surfaces, we prepared gold deposited PDMS substrates (see details in the Experimental section and ESI-2†). As revealed by optical and SEM images (Fig. 3(a)), the gold deposited PDMS surface shows complicated topological structures and is heterogeneous, with the coexistence of gold and unmodified PDMS surfaces. The gold deposited area is opaque and appears gray in the bright-field image. There are also surface features such as black wrinkles, corresponding to thicker gold regions, and white lines and small dots, corresponding to the transparent PDMS regions without gold deposition. The SEM image of the gold deposited surface further reveals the roughness of the surface. To increase the contrast of the surface charge, we modified the Au/PDMS substrates with 4-MBA or 4-ATP molecules (see the Experimental section and ESI-3†). The chemical modifications did not change the morphology of the substrates but endowed the substrates with different surface charges.

As shown in Fig. 3, we imaged the boundary regions of an Au/PDMS substrate modified with 4-MBA (4-MBA-Au/PDMS) using positive V_s with the small size nanopipette. The boundary region features both the rough gold deposited surface and flat PDMS surface, which can serve as the internal reference. Fig. 3(b) and (c) show both 3D topography and enhanced color topography images, respectively. The 3D topography image can better reveal the large height change of a sample and the enhanced color topography image can better reveal the local height difference with a large overall height change. For the enhanced color topography image in Fig. 3(c), the color of a pixel is determined by the height change compared to its neighbors. While the darker color represents a bigger height change, the relative height difference was colored in blue (lower surface region) and brown (higher surface region), respectively. The boundary line can be clearly visualized and is marked by a red line. In the gold deposited region at the left side, valleys and pits are the common features due to the electrochemical etching during gold deposition. The light brown areas are the PDMS domains without gold deposition.

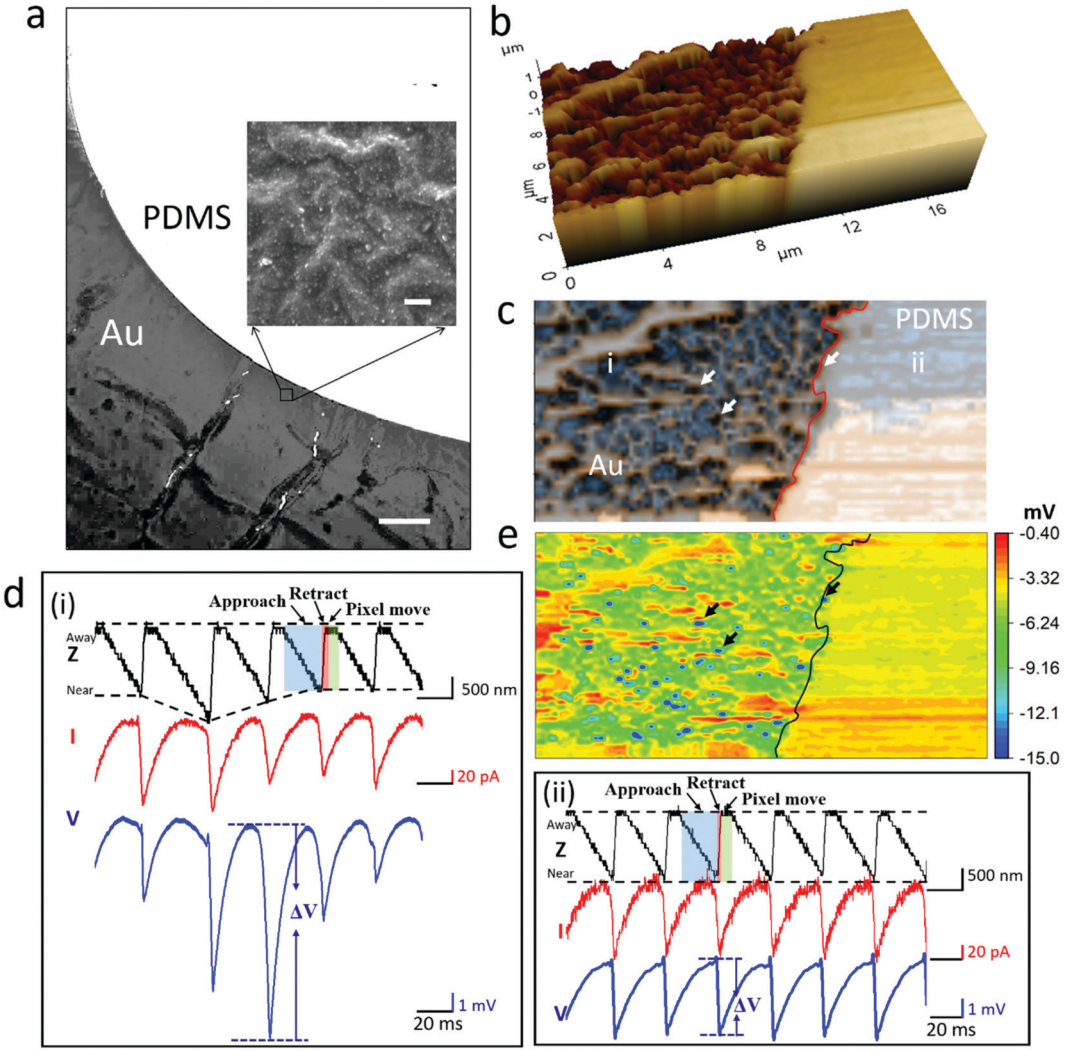

Fig. 3 Simultaneously recorded topography and surface potential maps of Au-coated PDMS modified with 4-MBA. (a) The bright-field optical microscopy image of an Au/PDMS substrate (scale bar: 4 μm). The inset shows a SEM image of the Au deposited area (scale bar: 1 μm). (b) A 3D topography image. (c) The corresponding enhanced color topography image. The red line indicates the boundary of the gold deposited PDMS area. (d) Simultaneously recorded time traces of displacement (*Z*), current (*I*), and potential (*V*) near sites i and ii indicated in (c). The blue, red, and green shaded regions in the *Z*–*t* trace indicate the approach, retract, and pixel move of the probe in a cycle. (e) The corresponding surface potential difference (Δ*V*) image. All the images are recorded at a positive sample bias with a small size nanopipette.

We quantified the surface roughness of the topography image using the surface area ratio.[27,35] The surface area ratio of PDMS surface without gold deposition (right side of the boundary line) is about 159 in a 5 × 5 μm^2 size, while that of the gold deposited PDMS region (left side) is around 456. The topography images are consistent with the optical and SEM images, suggesting that the SICM feedback system still works reasonably well on complicated surfaces.

During scanning, the time traces of *z*-piezo displacement (*Z*), current (*I*), and potential (*V*) were recorded using an oscilloscope and used for further analysis and Δ*V* image construction. To illustrate the principle of Δ*V* imaging using the ARS mode (see the Experimental section), the typical time traces of *Z*, *I* and *V* are presented in Fig. 3(d), taken from the sites (i) and (ii) marked in Fig. 3(c). Each pixel in the Δ*V* image was obtained from the potential difference at $D_{ps\text{-}min}$ and $D_{ps\text{-}max}$ after completing a cycle (*i.e.*, an approach–retract–pixel move) of the probe movement. The surface potential image constructed from the Δ*V* is robust against potential baseline drift and random noise.

In the *I*–*t* traces (see Fig. S8†), the average current drop is about 8.5%, which is due to the current overshoot of the probe on the complicated and soft surface. In contrast, the average current drop is about 2.2% on the flat PDMS surfaces (see Fig. S6†) and about 2.6% on the skin cell surface (see Fig. S14† and section 3.5). The bigger current overshoot is attributed to the slightly longer time delay of the feedback system on the rougher surface.

The surface charge of substrate slightly impacts the current drop magnitude. We typically observed a higher current drop

on the negative surface than on the positive surface. For example, on the flat PDMS surface, the average current drop is about 2.2% on the positive surface and about 2.4% on the negative surface (see Fig. S6(d and e)†). On the gold deposited PDMS surface, the average current drop is about 8.5% on the positive surface and about 8.7% on the negative surface (see Fig. S8†). The bigger current drop induces a smaller $D_{ps\text{-}min}$, making ΔV more negative. As shown in the FEM calculation, bigger ΔV magnitude can be obtained on the negative surface at the same $D_{ps\text{-}min}$. The dependence of $D_{ps\text{-}min}$ on the surface charge can further enlarge the difference of V response to different surface charges.

Because of the height dependence of V, the true extent of the influence of $D_{ps\text{-}min}$ on ΔV is unknown during image, considering the uncertainty of $D_{ps\text{-}min}$ at each pixel. Therefore, the crosstalk between the height and surface charge cannot be avoided in the ΔV image, especially on the rough surface. The ΔV signal is thus the convolution of both height and surface charge contributions. We can better understand this problem by investigating both the current and potential changes at a specific site. Compared with the V–t trace at site (ii) in the PDMS region, bigger ΔV changes are observed at site (i) in the gold deposition region. As shown in the I–t trace of site (i), the current drops more in the pit location, resulting in the bigger Z change in the Z–t trace and the corresponding variation of $D_{ps\text{-}min}$. However, the V change in the V–t trace does not exactly follow the changes in the I–t and Z–t traces. The bigger V change appears at the next pixel. In general, the V changes did not follow the I changes, as can be observed in additional traces shown in Fig. S6 and S8.† The different response of V and I suggests that ΔV is likely affected by both surface charge and $D_{ps\text{-}min}$.

Fig. 3(e) shows the corresponding ΔV image in the form of a heatmap. Examining both the topography and ΔV images, we can see that the most negative points (in blue) in the ΔV image appear in or around the pits in the topography image (as indicated by the arrows in Fig. 3(c) and (e)). The more negative potential at the pits can be attributed to both the probe height change and more molecules gathering in these holes, where more gold deposition occurs. Using positive V_s, the ΔV values are always negative but their magnitudes are obviously affected by the surface charge. The ΔV magnitude range and the contrast of ΔV image are both bigger on the negatively charged surface (4-MBA-Au) and smaller on the positively charged surface (4-ATP-Au). When a negative V_s is applied, the ΔV becomes positive and the contrast of ΔV image is greatly reduced. The examples are shown in ESI-8 and 9.† For the case of V_t, the contrast of ΔV images also show the same bias polarity dependence. Between the nanopipettes with different tip sizes, the small size nanopipette is more sensitive to small surface potential changes than the large size nanopipette. These results are consistent with the potential sensing mechanism we disused earlier, confirming that we can qualitatively reveal the surface charge distribution in ΔV imaging. In the following experiments, we always used positive V_s with a small size nanopipette, unless mentioned otherwise.

3.4 Mapping of the pH-dependent gold-deposited PDMS substrates

To further validate the surface charge sensing capability of the P-SICM on the rough surface, we altered the surface charge of 4-ATP- and 4-MBA modified Au/PDMS substrates by changing the pH value of the bath solution. 4-MBA is less negative at lower pH but more negative at higher pH, while 4-ATP is more positive at low pH (see ESI-4†).[36,37] Fig. 4 shows the results of topography (enhanced color), and ΔV images and histograms of 4-MBA-Au/PDMS at pH 9.6 (a), 4-MBA-Au/PDMS at pH 5.3 (b), 4-ATP-Au/PDMS at pH 9.6 (c), and 4-ATP-Au/PDMS at pH 5.3 (d) using V_s = +0.1 V with a small size nanopipette. These images were all taken near the boundary of the gold deposited PDMS region. In the ΔV image of Fig. 4(a), an increased number of blue dots appear in the gold deposited region. The ΔV values suggest these locations are more negative than other regions, likely induced by the mostly deprotonated carboxyl groups of 4-MBA at high pH. At pH 5.3, more green regions appear in the gold deposited area in the ΔV image of Fig. 4(b), suggesting the negative surface charge of gold is reduced at a lower pH. Compared with the topography image, the pH-dependent differences are not noticeable in the topography images but are obvious in the ΔV images. The corresponding ΔV histograms, constructed by the ΔV values at all pixels of the ΔV images, are shown at the right column. At pH 9.6, the ΔV distribution is broad and asymmetric with a large tail extending to the more negative side in the left. At pH 5.3, the ΔV distribution is much narrower but still asymmetric with more ΔV values distributed in the more negative side.

Fig. 4(c) and (d) show the topography and ΔV images of the 4-ATP-Au/PDMS substrate at pH 9.6 and 5.3, respectively. At pH 9.3, most of the gold deposited regions have the same green color as the PDMS in the ΔV image of Fig. 4(c), reflecting the neutralized charge of the amine group at pH 9.3. At pH 5.3, more orange regions appear in the gold deposited region in the ΔV image of Fig. 4(d). Most of these orange regions are the valleys and pits filled with gold, confirming that the 4-ATP modified gold surface become more positive than the PDMS surface at pH 5.3. This is due to the higher percentage of protonated amine groups of 4-ATP at lower pH. The ΔV histograms of 4-ATP modified surfaces at two pH values are both narrower than those of the 4-MBA case. At pH 5.6, the tail of the histogram extends slightly more towards the positive side in the right, as indicated by the red arrow. Statistically, the ΔV histogram should be similar for all the surfaces with the same level of surface roughness if the ΔV change is induced only by the current overshoot of the probe. The surface charge dependent change of ΔV images and histograms confirm that we can still map the surface charge distribution on the rough and soft substrates in the buffer by the P-SICM method.

3.5 Topography and extracellular surface potential mapping of live cell membranes

We then applied P-SICM to image the topography and extracellular potential distribution of living cell membranes. Here,

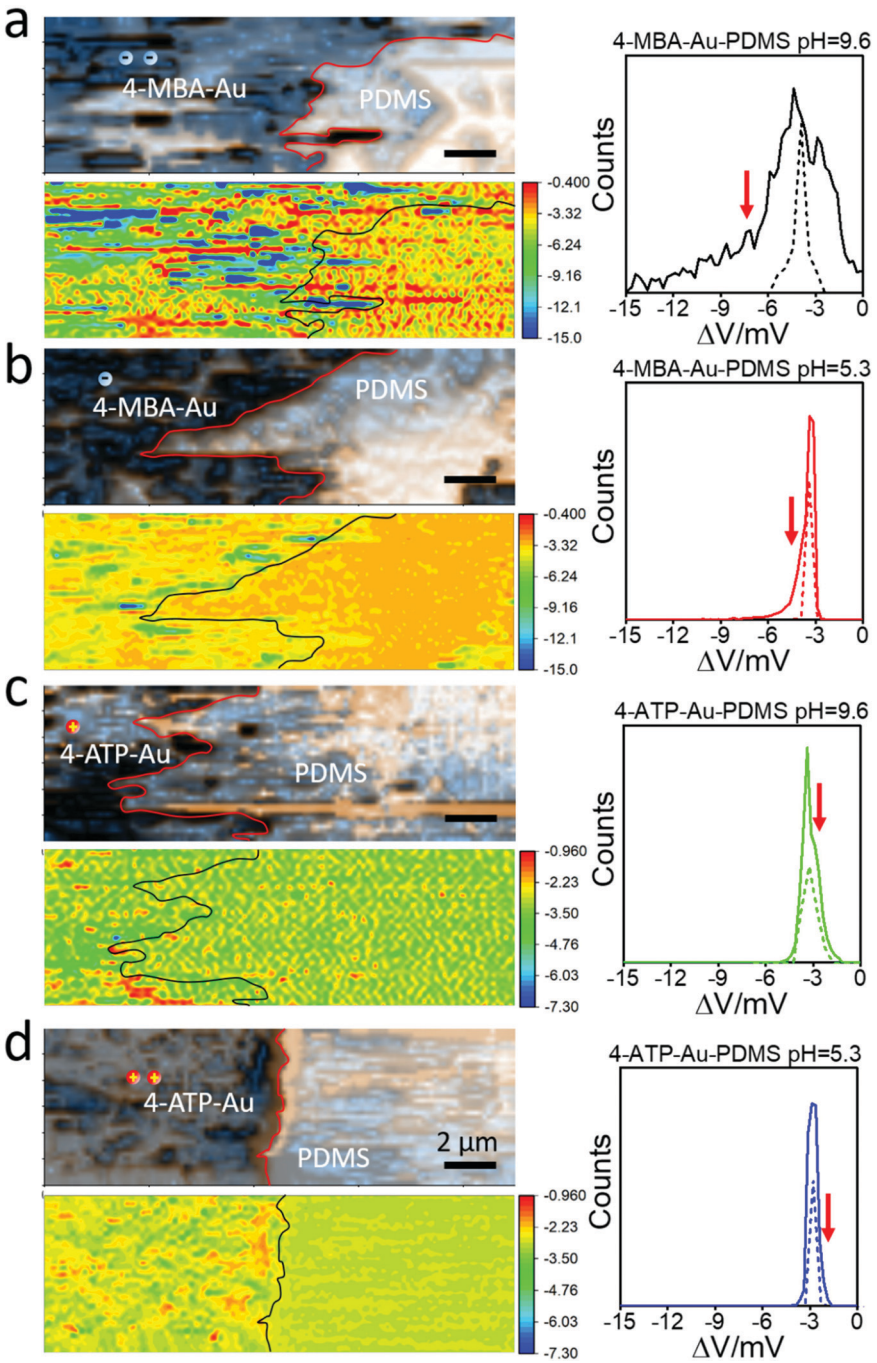

Fig. 4 Enhanced color topography and ΔV images (left column) and ΔV histograms (right column) of Au/PDMS substrates modified with 4-MBA or 4-ATP at different pH values in buffered solution using the positive sample bias mode (V_s = +0.1 V) with a small size nanopipette. (a–b) 4-MBA modified Au-PDMS at pH 9.6 (a) and 5.3 (b). (c–d) 4-ATP modified Au/PDMS at pH values of 9.6 (c) and 5.3 (d). The solid line histograms are constructed from the whole ΔV images and the dashed line histograms are constructed from the right side PDMS region without gold deposition.

melanocyte (Mela-A), the normal skin cell, and melanoma (B16), the cancerous skin cell are investigated. The viability of cells was examined by re-culturing the cells for 24 hours after P-SICM measurements. These cells can divide and show no difference under an optical microscope from cells that have not been imaged by P-SICM, suggesting that they were not obviously affected by P-SICM imaging. Fig. 5(a) and (b) show the simultaneously recorded 3D topography, enhanced color topography and ΔV images of Mela-A and B16 cells. The surface area ratio, a surface roughness indicator, of Mela-A is about 203.8, and the surface area ratio of B16 is slightly higher at around 235.8. They are bigger than that of flat PDMS surface but much smaller than that of the gold deposited PDMS surface, as discussed in section 3.3. The representative time

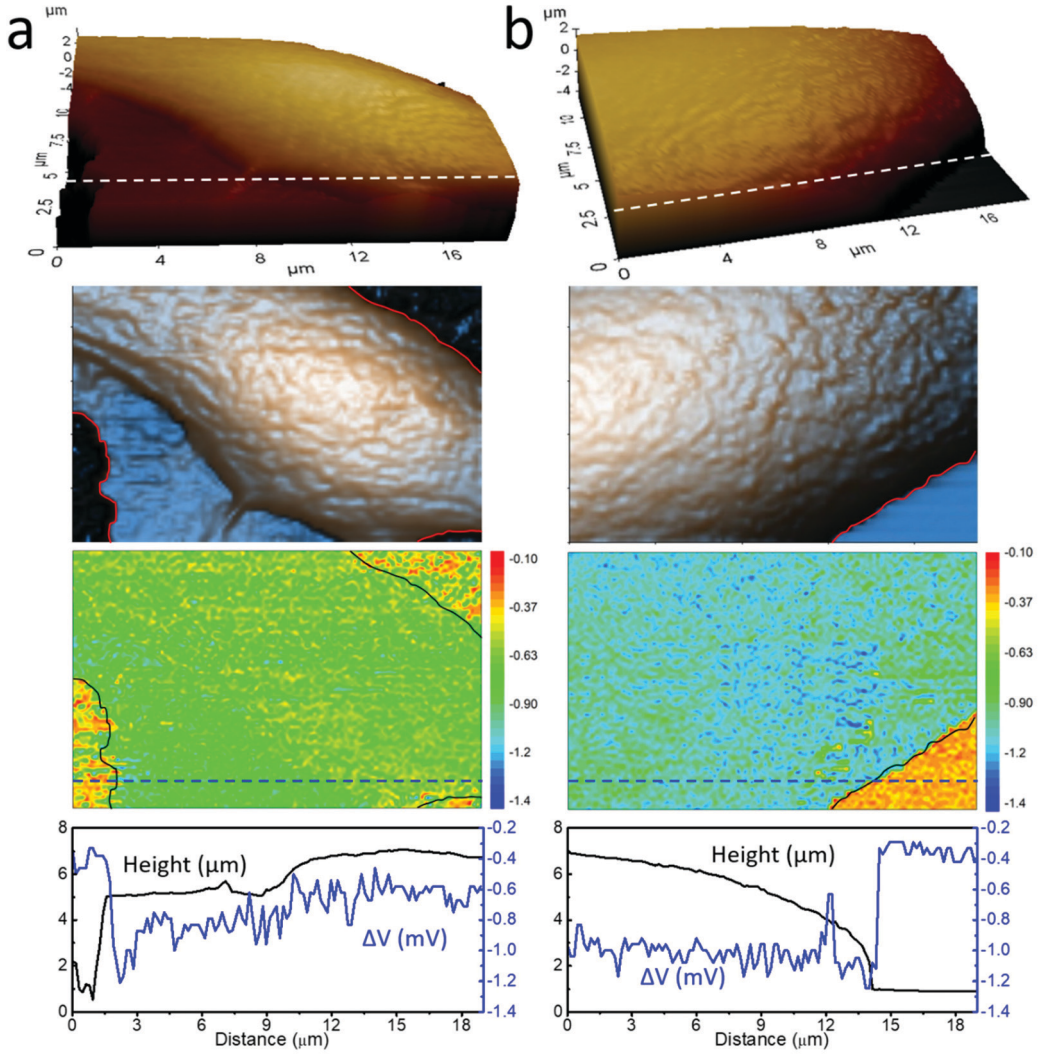

Fig. 5 Simultaneously recorded representative topography and ΔV images of Mela-A and B16 live cells in HEPES buffer with 5 mM K^+. (a–b) 3D Topography (top), enhanced color topography (the second row), and ΔV images (the third row) of Mela-A (a) and B16 (b). Height and ΔV profiles (bottom) are across the white and blue dashed lines, respectively. The images were collected using the sample bias mode (V_s = +0.1 V) with a small size nanopipette of 60 nm diameter.

traces of Z, I and V during SICM imaging are shown in Fig. S14.† The feedback system of SICM performs relatively well on the skin cell surface, with a uniform current drop in the range of 2.6–2.8%. The ΔV images reveal that the cell surface is more negative than the fibronectin modified PDMS substrate (reddish regions in the corners of both ΔV images). Here, the surface of B16 is slightly more negative than the surface of Mela-A. The mean ΔV is −0.94 mV for Mela-A cells and −1.04 mV for B16 cells. The surface potential distribution was generally uniform, and no obvious heterogeneity was observed in both ΔV images. The height and ΔV profiles along the dashed lines drawn in the images further show the detailed changes of the height and potential across the fibronectin modified PDMS substrate and the cell surface. The cell membrane surface is relatively smooth while the cell height is up to 6 μm.

We also carried out experiments to monitor extracellular membrane potential changes of Mela-A and B16 in HEPES buffers with different K^+ concentrations ($[K^+]$). $[K^+]$ in the extracellular solution is a critical determinant of the resting membrane potential of cells and must be maintained within a narrow range, normally between 3.5 and 5 mM. Reduction of $[K^+]$ is associated with hyperpolarization of the resting membrane potential, while depolarization effects are seen when the $[K^+]$ is increased.[38] Zhou *et al.* have reported that the trans membrane potential can be dramatically depolarized by increasing the extracellular $[K^+]$.[39] To increase the extracellular $[K^+]$, we replaced the sodium ion with potassium ion in the HEPES buffer while maintaining the same ionic strength. Same measurements were carried out for both Mela-A and B16 with $[K^+]$ values of 5, 25, 45, and 60 mM. Fig. S13† shows the typical bright-field optical microscopy images of cells treated

with different extracellular K^+ concentrations in HEPES buffer. It is noticeable that the image contrast and resolution are reduced with the increase of extracellular $[K^+]$. We speculate that this is due to the increased membrane permeability after exposure to higher $[K^+]$, though no direct proof has been obtained. However, the treatment with 60 mM $[K^+]$ for prolonged time often led to the death of cells.

Fig. 6 shows the topography (enhanced color) and ΔV images of the cell membrane after exposure to different $[K^+]$ for about 10 min. In the topographic images for both types of cells, noticeable changes only appear at 60 mM, with wrinkles on the roughed surfaces. Obvious changes were observed in the corresponding potential images. With the increase of $[K^+]$, the color of ΔV images gradually changes from yellow/orange to green/blue. The ΔV images are generally featureless with uniform ΔV distribution at lower $[K^+]$. Starting from 45 mM, a clear color change is observed as the ΔV becomes more negative (green or blue) during the scanning from the bottom to the top in a time span of 15 min. The dramatic changes with bigger color contrast in ΔV images appear at 45 mM for Mela-A and 60 mM for B16. The representative Z–t, I–t and V–t traces at 60 mM are shown in Fig. S14(c).† The average current drop slightly increases to about 3.2%, reflecting a more negative cell surface at 60 mM. The current drop is uniform in the I–t trace but the ΔV changes are obviously bigger in the V–t trace. Therefore, the cross talk between the height and V signal is small and the ΔV change is mainly induced by the surface charge/potential change. In control experiments under the same conditions, the $[K^+]$ changes of the bath solution did not affect the ΔV images when no cells were added to the fibronectin modified PDMS.

The $[K^+]$ dependent changes of ΔV images suggest that the cell membrane is more negative at higher $[K^+]$, which is mainly attributed to the change in the electrostatic properties of the cell membrane after prolonged exposure to high $[K^+]$. The more permeable membrane may expose the negative interior of cells[40] and allow the rerelease of more cellular contents. The lipid surface may also become more negative, triggered by membrane depolarization,[39] though further investigations are needed. The increased contrast of ΔV images likely suggests that the membrane damage process triggered by elevated $[K^+]$ is inhomogeneous. The regions in green (in the bottom half of the ΔV image at 45 mM in Fig. 5(a)) or blue (in the top half of the ΔV image at 60 mM in Fig. 5(c)) are likely damaged first as a result of a higher membrane permeability. Later the whole cell membrane is damaged and the ΔV image becomes homogeneous again, showing more negative mean ΔV values (see the ΔV image at 60 mM in Fig. 5(a)). Based on the ΔV images, the membrane of the B16 cell is less damaged at 60 mM than the membrane of Mela-A. Therefore, the cancer cell B16 is slightly more resistant to elevated extracellular $[K^+]$. Fig. 6(b) and (d) show the bar graph of mean membrane surface poten-

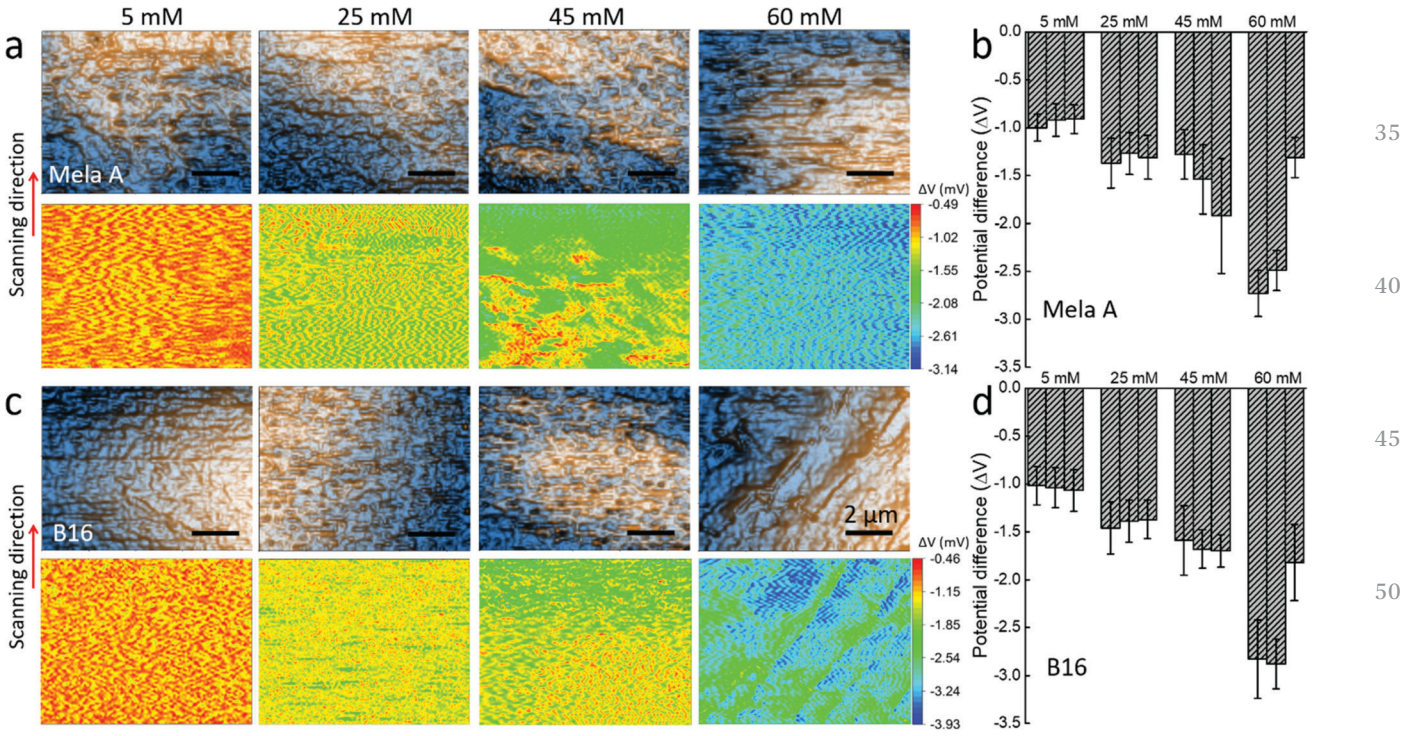

Fig. 6 Simultaneously recorded topography and ΔV images of Mela-A and B16 live cells at different extracellular K^+ concentrations in HEPES buffer. (a) Enhanced color topography (top panel) and ΔV images (bottom panel) of Mela-A cells. (b) The bar graph of ΔV for three batch of Mela-A cells at different extracellular $[K^+]$. The error bar of each bar reflects the fluctuations of ΔV from at least two cell samples. (c) Enhanced color topography (top panel) and ΔV images (bottom panel) of B16 cells. (d) The bar graph of ΔV for three batches of B16 cells at different extracellular $[K^+]$.

tial ΔV of Mela-A and B16 cells treated at various extracellular $[K^+]$. To include variations from cell to cell and batch to batch, we collected the average ΔV data from at least two cells of each batch and repeated this for at least three batches. The Mela-A cells showed slightly more negative ΔV mean values at 45 mM. A sudden increase of ΔV magnitude appeared at 60 mM for both types of cells, indicating that the cell is severely damaged. These live cell experiments confirm that we can simultaneously monitor the dynamic changes of the cell membrane structure and surface potential of a living cell by the P-SICM imaging method.

4. Conclusions

In summary, we have developed a P-SICM imaging technique using a dual-barrel nanopipette, which can simultaneously map the topography and surface charge/potential distribution on living cell membranes. We first demonstrated the surface charge/potential mapping capability of P-SICM on flat PDMS substrates. In the next step, the P-SICM was evaluated to image soft and spiky PDMS surfaces, which were prepared by partially coating with gold by electrochemical deposition, following chemical modifications of the gold deposited surface. The systematic studies on PDMS substrates with different topologies and surface charges demonstrate that P-SICM could detect sub-millivolt potential changes with the distance between the nanopipette tip and substrate of up to 200 nm; the probe with a smaller pore diameter showed a higher spatial resolution and potential sensitivity; and the quality of the potential image is higher using a positive sample bias. The experimental results were then confirmed by FEM simulations. However, we also found that the height-control by SICM is less accurate on rough surfaces, leading to the reduced accuracy of potential measurement. Using a positive sample bias and small size nanopipette, we have acquired the topography and surface potential images of the membrane of normal and cancerous skin cells. The P-SICM performs well on these relatively smooth cell surfaces. When exposed to the elevated potassium ion concentration in the bath solution, the cancer cell can endure a slightly higher extracellular potassium ion concentration. We also observed obvious heterogeneous domains in the potential image, which are attributed to the possible membrane damage induced by the elevated extracellular potassium concentration. The new P-SICM method reported here provides a new tool for cell membrane studies. Although the crosstalk between height and potential somewhat limited the accuracy of the acquired potential image, especially when the height control is compromised on complicated substrates, P-SICM can still provide a valuable means to map the surface charge/potential distribution on soft live cell membranes. With the continued progress of SICM feedback control, we also expect that the accuracy of the potential imaging can be further improved. The P-SICM method will also benefit the electrophysiology and bioelectricity studies and complement the current electrode-based techniques, such as patch-clamp or microelectrode arrays (MEAs) methods, to provide high spatial resolution and measure slow and long-term electrical changes of non-excitable live cells.

Conflicts of interest

There are no conflicts to declare.

Acknowledgements

This work was supported by FIU BSI sandbox to J. H. and L. K. and National Science Foundation (NSF, CBET1454544) to J. H. This work was also partially supported by the ERC program of NSF under NSF Cooperative Agreement No. EEC-1647837. F. C. would like to thank the support from CSC fellowship. X. S. L. and N. P. also acknowledge the support from FIU DYF fellowship. We also thank Alberto Ribfiaro for control experiments.

Notes and references

1 T. Ushiki, M. Nakajima, M. Choi, S. J. Cho and F. Iwata, *Micron*, 2012, **43**, 1390–1398.
2 J. Seifert, J. Rheinlaender, P. Novak, Y. E. Korchev and T. E. Schäffer, *Langmuir*, 2015, **31**, 6807–6813.
3 P. Hansma, B. Drake, O. Marti, S. Gould and C. Prater, *Science*, 1989, **243**, 641–643.
4 C. B. Prater, P. K. Hansma, M. Tortonese and C. F. Quate, *Rev. Sci. Instrum.*, 1991, **62**, 2634–2638.
5 Y. Korchev, C. Bashford, M. Milovanovic, I. Vodyanoy and M. Lab, *Biophys. J.*, 1997, **73**, 653–658.
6 T. E. Schaffer, *Anal. Chem.*, 2013, **85**, 6988–6994.
7 P. Novak, A. Shevchuk, P. Ruenraroengsak, M. Miragoli, A. J. Thorley, D. Klenerman, M. J. Lab, T. D. Tetley, J. Gorelik and Y. E. Korchev, *Nano Lett.*, 2014, **14**, 1202–1207.
8 G. A. Robertson, *Circ. Res.*, 2013, **112**, 1088–1090.
9 R. A. Lazenby, K. McKelvey and P. R. Unwin, *Anal. Chem.*, 2013, **85**, 2937–2944.
10 M. Shen, R. Ishimatsu, J. Kim and S. Amemiya, *J. Am. Chem. Soc.*, 2012, **134**, 9856–9859.
11 Y. Takahashi, Y. Zhou, T. Miyamoto, H. Higashi, N. Nakamichi, Y. Takeda, Y. Kato, Y. Korchev and T. Fukuma, *Anal. Chem.*, 2020, **92**, 2159–2167.
12 A. I. Shevchuk, J. Gorelik, S. E. Harding, M. J. Lab, D. Klenerman and Y. E. Korchev, *Biophys. J.*, 2001, **81**, 1759–1764.
13 Y. E. Korchev, Y. A. Negulyaev, C. R. W. Edwards, I. Vodyanoy and M. J. Lab, *Nat. Cell Biol.*, 2000, **2**, 616–619.
14 K. McKelvey, S. L. Kinnear, D. Perry, D. Momotenko and P. R. Unwin, *J. Am. Chem. Soc.*, 2014, **136**, 13735–13744.
15 N. Schierbaum, M. Hack, O. Betz and T. E. Schäffer, *Anal. Chem.*, 2018, **90**, 5048–5054.

16 H. Ida, Y. Takahashi, A. Kumatani, H. Shiku and T. Matsue, *Anal. Chem.*, 2017, **89**, 6015–6020.

17 S. Simeonov and T. E. Schäffer, *Nanoscale*, 2019, **11**, 8579–8587.

18 A. Page, D. Perry and P. R. Unwin, *Proc. R. Soc. A*, 2017, **473**.

19 D. Momotenko, K. McKelvey, M. Kang, G. N. Meloni and P. R. Unwin, *Anal. Chem.*, 2016, **88**, 2838–2846.

20 C. A. Morris, C.-C. Chen and L. A. Baker, *Analyst*, 2012, **137**, 2933–2938.

21 Y. Zhou, L. K. Bright, W. Shi, C. A. Aspinwall and L. A. Baker, *Langmuir*, 2014, **30**, 15351–15355.

22 D. Perry, B. Paulose Nadappuram, D. Momotenko, P. D. Voyias, A. Page, G. Tripathi, B. G. Frenguelli and P. R. Unwin, *J. Am. Chem. Soc.*, 2016, **138**, 3152–3160.

23 L. H. Klausen, T. Fuhs and M. Dong, *Nat. Commun.*, 2016, **7**, 12447.

24 D. Perry, B. Paulose Nadappuram, D. Momotenko, P. D. Voyias, A. Page, G. Tripathi, B. G. Frenguelli and P. R. Unwin, *J. Am. Chem. Soc.*, 2016, **138**, 3152–3160.

25 A. Page, D. Perry, P. Young, D. Mitchell, B. G. Frenguelli and P. R. Unwin, *Anal. Chem.*, 2016, **88**, 10854–10859.

26 Y. Zhou, C.-C. Chen, A. E. Weber, L. Zhou and L. A. Baker, *Langmuir*, 2014, **30**, 5669–5675.

27 F. Chen, P. Manandhar, M. S. Ahmed, S. Chang, N. Panday, H. Zhang, J. H. Moon and J. He, *Macromol. Biosci.*, 2019, **19**, 1800271.

28 P. Novak, C. Li, A. I. Shevchuk, R. Stepanyan, M. Caldwell, S. Hughes, T. G. Smart, J. Gorelik, V. P. Ostanin, M. J. Lab, G. W. Moss, G. I. Frolenkov, D. Klenerman and Y. E. Korchev, *Nat. Methods*, 2009, **6**, 279–281.

29 P. Novak, C. Li, A. Shevchuk, R. Stepanyan, M. Caldwell, S. Hughes, T. Smart, J. Gorelik, V. Ostanin, M. Lab, G. Moss, G. Frolenkov, D. Klenerman and Y. Korchev, *Nat. Methods*, 2009, **6**, 279–281.

30 G. E. Jung, H. Noh, Y. K. Shin, S. J. Kahng, K. Y. Baik, H. B. Kim, N. J. Cho and S. J. Cho, *Nanoscale*, 2015, **7**, 10989–10997.

31 J. Zhuang, L. Cheng, X. Liao, A. A. Zia and Z. Wang, *Rev. Sci. Instrum.*, 2020, **91**, 033703.

32 H. J. Bai, M. L. Shao, H. L. Gou, J. J. Xu and H. Y. Chen, *Langmuir*, 2009, **25**, 10402–10407.

33 E. V. Sviderskaya, S. P. Hill, T. J. Evans-Whipp, L. Chin, S. J. Orlow, D. J. Easty, S. C. Cheong, D. Beach, R. A. DePinho and D. C. Bennett, *J. Natl. Cancer Inst.*, 2002, **94**, 446–454.

34 Z. G. Peng, K. Hidajat and M. S. Uddin, *J. Colloid Interface Sci.*, 2004, **271**, 277–283.

35 Y. Shan, N. Panday, Y. Myoung, M. Twomey, X. Wang, W. Li, E. Celik, V. Moy, H. Wang, J. H. Moon and J. He, *Macromol. Biosci.*, 2016, **16**, 599–607.

36 Y. Feng, Y. Wang, H. Wang, T. Chen, Y. Y. Tay, L. Yao, Q. Yan, S. Li and H. Chen, *Small*, 2012, **8**, 246–251.

37 H. Fang, H. J. Yin, M. Y. Lv, H. J. Xu, Y. M. Zhao, X. Zhang, Z. L. Wu, L. Liu and T. W. Tan, *Biosens. Bioelectron.*, 2015, **69**, 71–76.

38 R. Bouchard, R. B. Clark, A. E. Juhasz and W. R. Giles, *J. Physiol.*, 2004, **556**, 773–790.

39 Y. Zhou, C.-O. Wong, K.-J. Cho, D. van der Hoeven, H. Liang, D. P. Thakur, J. Luo, M. Babic, K. E. Zinsmaier, M. X. Zhu, H. Hu, K. Venkatachalam and J. F. Hancock, *Science*, 2015, **349**, 873–876.

40 S. McLaughlin, *Annu. Rev. Biophys. Biophys. Chem.*, 1989, **18**, 113–136.